The electronic band structure of polar polymorph α/β-BaTeMo$_2$O$_9$ phases

A.H. Reshak [a, b, *]

[a] New Technologies — Research Centre, University of West Bohemia, Univerzitni 8, 306 14 Pilsen, Czech Republic
[b] Center of Excellence Geopolymer and Green Technology, School of Material Engineering, University Malaysia Perlis, 01007 Kangar, Perlis, Malaysia

A B S T R A C T

Based on the reported experimental geometrical structure, a comprehensive theoretical calculations were performed to investigate the electronic band structure, the angular momentum projected density of states, the electronic charge density distribution and the chemical bonding characters of α-BaTeMo$_2$O$_9$ and β-BaTeMo$_2$O$_9$. Calculation reveals that in both phases the conduction band minimum (CBM) is located at Γ point of first Brillouin zone (BZ) whereas the valence band maximum (VBM) of β-BaTeMo$_2$O$_9$ phase is situated in the mid way between Z and Γ points of BZ, while it is located at Z point for α-BaTeMo$_2$O$_9$ phase, resulting in an indirect band gap of about 2.93 eV (β) and 3.12 eV (α) in good agreement with the measured values 2.95 eV (β) and 3.12 eV (α). It has been noticed that the VBM is mainly formed by O-p states while the CBM is controlled by Mo-d state. The valence band's electronic charge density distribution reveals that β-BaTeMo$_2$O$_9$ phase show there exists a strong covalent bonding between Mo and O also between Te and O atoms, while Ba atom forms mostly ionic and partially covalent bonding with O atom. The phase transition from β → α cause to perturb the interaction between Mo and O atoms, Te and O atoms and Ba and O atoms which is attributed to the different arrangement between the atoms of the two phases, where the asymmetric unit of β-phase have a formula BaTeMo$_2$O$_9$ while for α-phase the asymmetric unit have the formula Ba$_2$Te$_2$Mo$_4$O$_{18}$. Due to the electro-negativity difference between the atoms we can see a charge transfer towards O atoms as indicated by the blue color around O atoms. The calculated bond lengths and angles show good agreement with the experimental values. The good agreement with experimental data in the matter of lattice parameters, energy gap values, the bond lengths and angles reveals the accuracy of the selected exchange correlation potentials used here.

© 2015 Elsevier B.V. All rights reserved.

1. Introduction

Due to their unique properties, the inorganic oxide became technologically important. The inorganic oxides are potential candidates for several applications, such as piezoelectricity, ferroelectricity and pyroelectricity [1]. Some of the inorganic oxide synthesized in noncentrosymmetric structure which give them considerable interest as second order nonlinear optical materials [2–7]. Therefore, several polar oxides single crystals have been synthesized [8–11]. The search for new polar materials is of current interest. Recently Zhang et al. [2] investigated the suitability of polar oxides containing cations susceptible to second order

Jahn–Teller distortions for nonlinear optical and piezoelectric application. They discovered a novel polar polymorph α-BaTeMo$_2$O$_9$ during the growing β-BaTeMo$_2$O$_9$ single crystal, it has been found that at temperature below 570 °C the product is only β-BaTeMo$_2$O$_9$ while at 570 °C a small amount of α-BaTeMo$_2$O$_9$ appears and above 570 °C the product was pure α-BaTeMo$_2$O$_9$ [2]. Zhang et al., reported that both phases are thermally stabile and crystallized in noncentrosymmetric structure. After the discovery of α-BaTeMo$_2$O$_9$ phase several research groups reported the unique properties of the newly discovered phase [3,7,12]. Liu et al. [12] have reported Raman spectra of α-BaTeMo$_2$O$_9$ using pulsed laser diode pumped Nd:YAG/Cr^{4+}:YAG. Majchrowski et al. [3] studied the optical second harmonic generation at fundamental wavelength of 1064 nm under photoinducing treatment of monoclinic piezoelectric β-BaTeMo$_2$O$_9$. They have used two continuous wave lasers 808 and 1064 nm as photoinducing sources. Recently Gao et al. [7] theoretically investigated the refractive index and the birefringence

---

of α-BaTeMo$_2$O$_9$ in the spectral range of 0.4–5.0 μm. They have used a plane-wave pseudopotential total energy package CASTEP within the generalized gradient approximation (PBE–GGA).

Even though there exists some experimental and theoretical investigation on β-BaTeMo$_2$O$_9$ and α-BaTeMo$_2$O$_9$ [2,3,10–12] we feel that there is a dearth information on the electronic band structure, the electron charge density distribution, density of states and the contributions of each atom in β-BaTeMo$_2$O$_9$ and α-

BaTeMo$_2$O$_9$ phases and the influence of the phase transition from $\beta \rightarrow \alpha$ on the ground states properties of these phases. To the best of our knowledge no comprehensive work neither experimental data or first principles calculations to investigate the influence of the phase transition from $\beta \rightarrow \alpha$ on the electronic band structure, density of states and the electronic charge distribution of the two phases β-BaTeMo$_2$O$_9$ and α-BaTeMo$_2$O$_9$ have appeared in the literature. Therefore, we thought it is worthwhile to perform
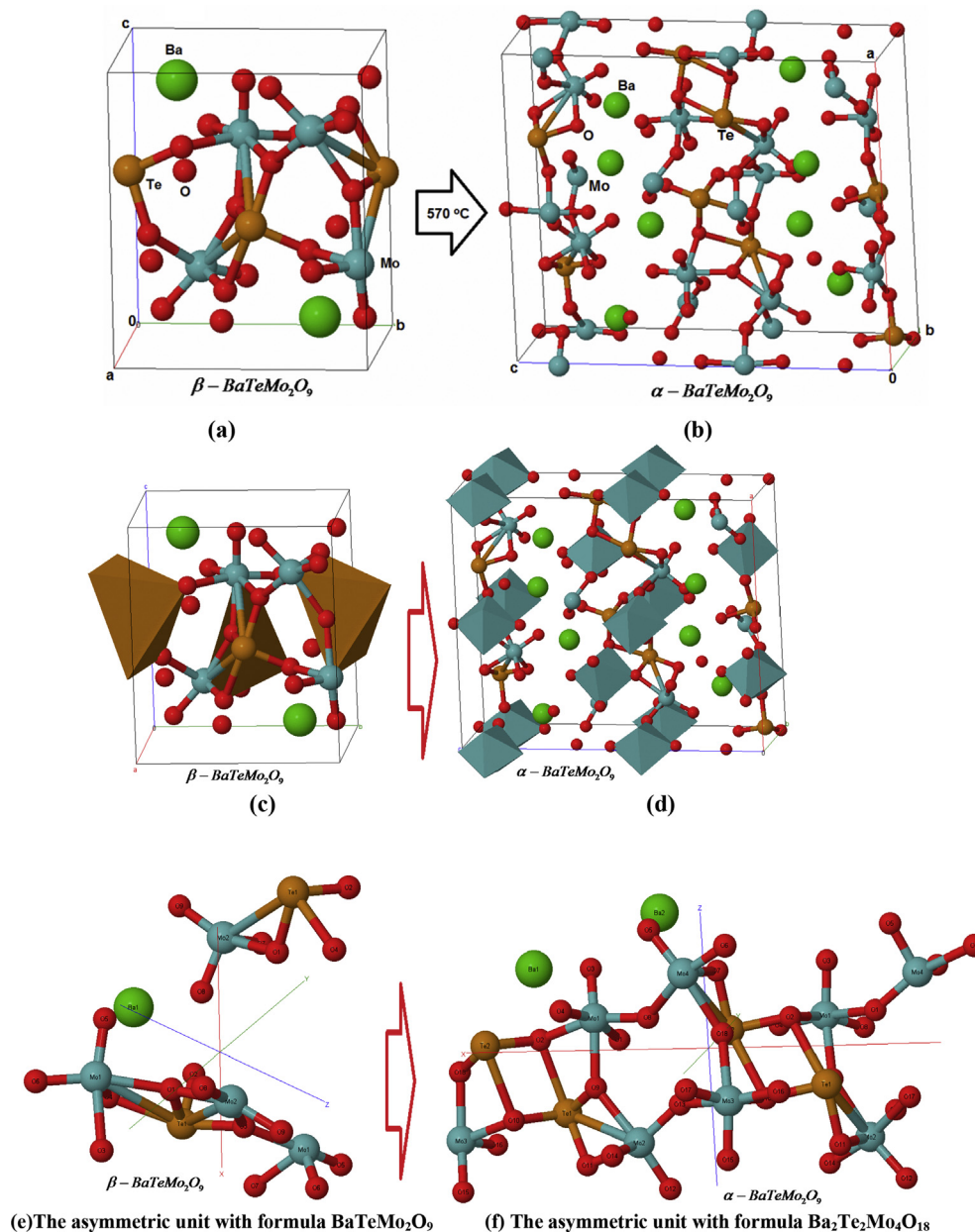
Fig. 1. **(a)**–**(b)** The crystal structure of β-BaTeMo$_2$O$_9$ and α-BaTeMo$_2$O$_9$. In the unit cell of α-phase the length of two axes are almost double of that in β-phase. β-BaTeMo$_2$O$_9$ and α-BaTeMo$_2$O$_9$ are 2D layered structures. β-phase consist of two symmetry independent MoO$_6$ octahedra and one TeO$_4$ polyhedra which interconnect to form the 2D anionic layer, while α-phase contains TeO$_3$, TeO$_4$ polyhedra and MoO$_6$ octahedra, the MoO$_6$ combine with three nearest neighbor MoO$_6$ through the corners to form 1D-zigzag chain of the tetramer Mo$_4$O$_{20}$. The resulting Mo$_4$O$_{20}$ linked to TeO$_3$ and TeO$_4$ to form the 2D anionic layer with Ba^{2+} cations located between the layers; **(c)**–**(d)** Polyhedral of β-BaTeMo$_2$O$_9$ and α-BaTeMo$_2$O$_9$; **(e)** The asymmetric unit of β-BaTeMo$_2$O$_9$ with formula **BaTeMo$_2$O$_9$**. In β-BaTeMo$_2$O$_9$ phase the Te(1)O$_4$ polyhedra is formed between Te(1) with O(1), O(2), O(3) and O(4), and the two Mo(1)O$_6$ octahedra is formed between Mo(1) and O(1), O(3), O(4), O(5), O(6), O(7), the second Mo(2)O$_6$ octahedra is formed between Mo(2) and O(1), O(2), O(3), O(7), O(8), O(9); **(f)** The asymmetric unit of α-BaTeMo$_2$O$_9$ with formula **Ba$_2$Te$_2$Mo$_4$O$_{18}$**. In α-BaTeMo$_2$O$_9$ the Te(1)O$_4$ polyhedra is formed between Te(1) with O(2), O(9), O(10) and O(11), the second Te(1)O$_4$ polyhedra is formed between Te(1) with O(7), O(8), O(10) and O(11), the Te(2)O$_3$ polyhedra is formed between Te(2) with O(2), O(7) and O(18), the three Mo(1)O$_6$ octahedra is formed between Mo(1) and O(1), O(2), O(3), O(4), O(8), O(9), the second Mo(2)O$_6$ octahedra is formed between Mo(2) and O(9), O(11), O(12), O(13), O(14), O(17), the third Mo(3)O$_6$ octahedra is formed between Mo(3) and O(10), O(13), O(15), O(16), O(17), O(18) and the fourth Mo(4)O$_6$ octahedra is formed between Mo(4) and O(1), O(5), O(6), O(7), O(8), O(18).

Table 1
The optimized atomic position of α-BaTeMo$_2$O$_9$ phase in comparison with the experimental data [2].

α-BaTeMo$_2$O$_9$

	x exp.	x opt.	y exp.	y opt.	z exp.	z opt.
Mo1	0.74289	0.7401	0.51943	0.5192	0.57244	0.5722
Mo2	0.6627	0.6611	0.52207	0.5221	0.35036	0.3504
Mo3	0.50978	0.5100	1.01397	1.0140	0.39096	0.3911
Mo4	0.58844	0.5880	1.02435	1.0240	0.6131	0.6132
Ba1	0.83844	0.8391	0.02469	0.0245	0.70106	0.7012
Ba2	0.59128	0.5912	0.50931	0.5089	0.76276	0.7629
Te1	0.78801	0.7881	0.14791	0.1480	0.42582	0.4259
Te2	0.96657	0.9664	0.35712	0.3572	0.53877	0.5397
O1	0.66938	0.6691	0.17201	0.1722	0.5575	0.5573
O2	0.84435	0.8439	0.25779	0.2580	0.55351	0.5533
O3	0.739	0.7391	0.44052	0.4401	0.66835	0.6682
O4	0.82445	0.8240	0.73645	0.7360	0.57134	0.5712
O5	0.64849	0.6481	0.95307	0.9532	0.69464	0.6944
O6	0.51715	0.5169	1.24985	1.2495	0.64237	0.6424
O7	0.99483	0.9941	0.24633	0.2460	0.63791	0.6378
O8	0.6413	0.6413	0.67947	0.6789	0.56148	0.5613
O9	0.74308	0.7429	0.45303	0.4532	0.45316	0.4533
O10	0.90867	0.9085	0.25366	0.2531	0.41005	0.4101
O11	0.7571	0.7572	0.25523	0.2550	0.32612	0.3260
O12	0.59894	0.5988	0.44974	0.4498	0.27085	0.2709
O13	0.58481	0.5849	0.67902	0.6792	0.40732	0.4072
O14	0.734	0.7342	0.74223	0.7422	0.31736	0.3172
O15	0.51293	0.5128	0.94387	0.9439	0.29492	0.2942
O16	0.42422	0.4241	1.22269	1.2225	0.39342	0.3931
O17	0.60892	0.6088	0.18337	0.1832	0.40212	0.4021
O18	0.5089	0.5090	0.94993	0.9493	0.5116	0.5117

Table 2
The optimized atomic position of β-BaTeMo$_2$O$_9$ phase in comparison with the experimental data [2,17].

β-BaTeMo$_2$O$_9$

|	x exp.	x opt.	y exp.	y opt.	z exp.	z opt.
Te1	0.61819	0.6185	0.51462	0.5146	0.42583	0.4257
Mo1	0.22569	0.2257	0.27524	0.2750	0.22768	0.2277
Mo2	−0.2078	0.7922	0.95108	0.9511	0.32593	0.3258
Ba1	0.27776	0.2777	0.7445	0.7439	0.06721	0.0672
O1	0.2899	0.2889	0.4313	0.4311	0.4392	0.4390
O2	0.5395	0.5391	0.7318	0.7316	0.3326	0.3329
O3	0.5472	0.5470	0.5946	0.5942	0.6309	0.6310
O4	0.5038	0.5040	0.3952	0.3949	0.1895	0.1891
O5	0.0152	0.0150	0.4316	0.4315	0.1644	0.1641
O6	0.2227	0.2224	0.1182	0.1180	0.082	0.0822
O7	−0.0284	0.9716	0.1531	0.1528	0.3596	0.3592
O8	0.0194	0.0190	0.7937	0.7932	0.3334	0.3333
O9	−0.2797	0.7203	0.9651	0.9650	0.1337	0.1336
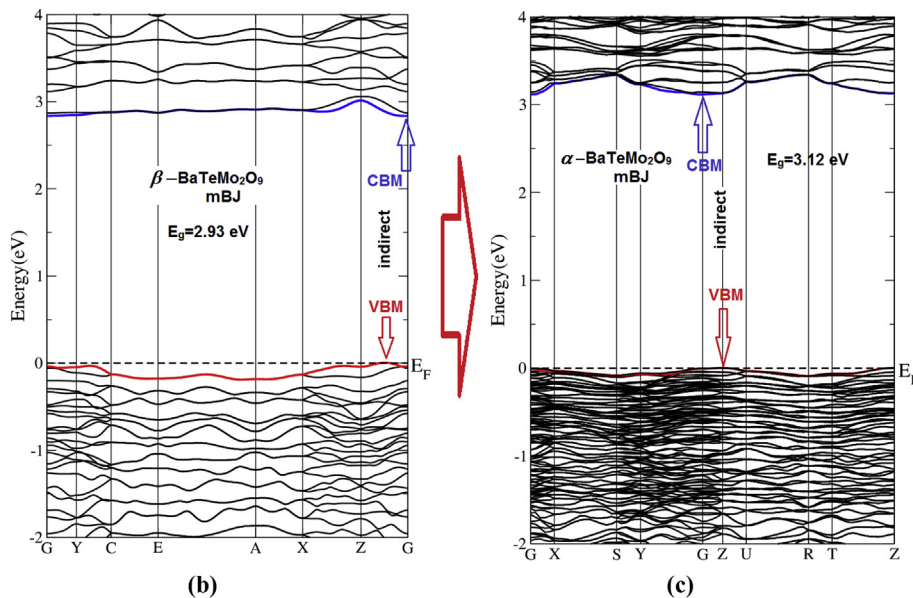
Fig. 2. Calculated electronic band structure of β-BaTeMo$_2$O$_9$ and α-BaTeMo$_2$O$_9$ using mBJ.
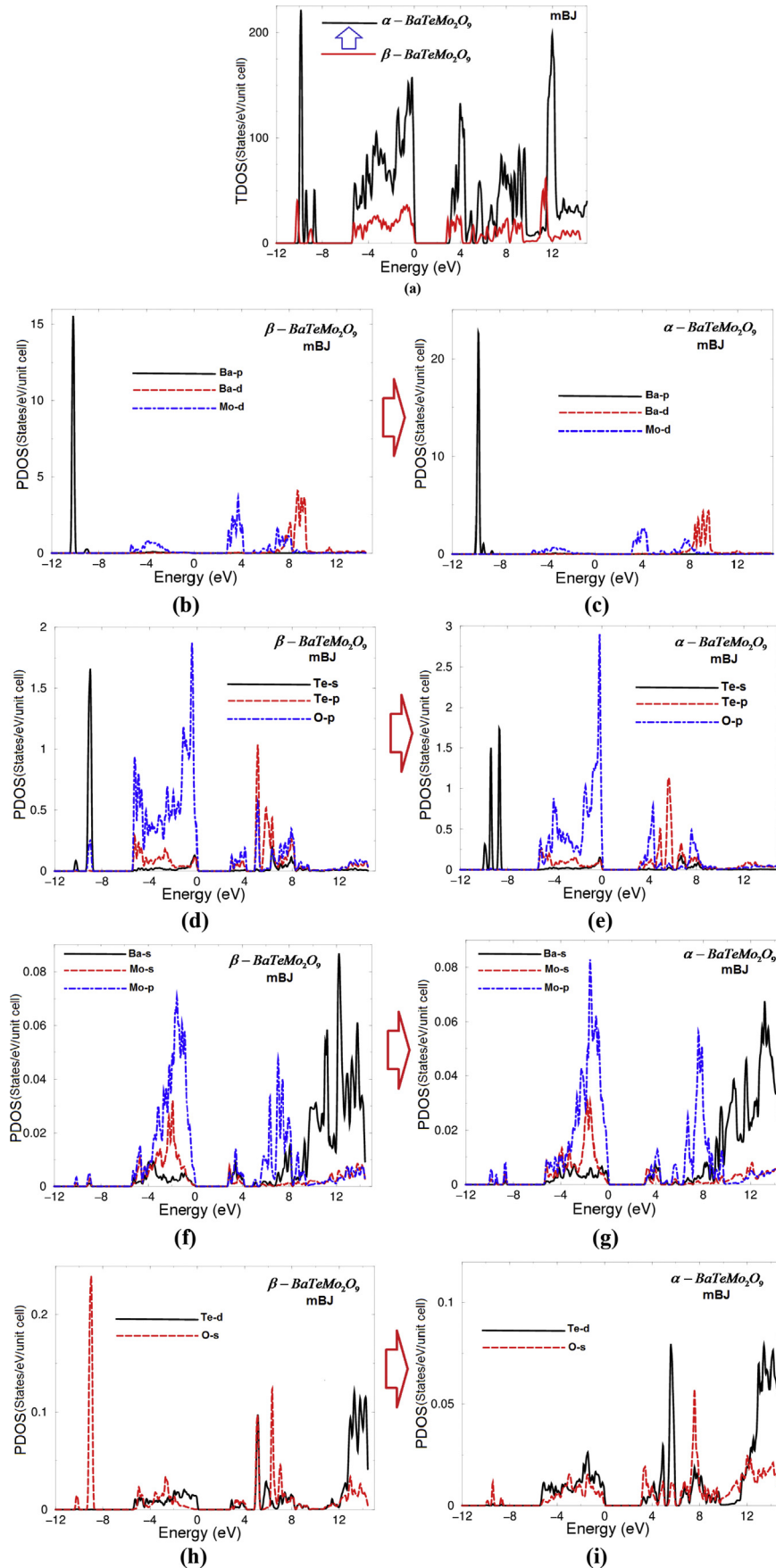
Fig. 3. Calculated total and partial density of states of β–BaTeMo$_2$O$_9$ and α–BaTeMo$_2$O$_9$ using mBJ.

comprehensive theoretical calculation based on the density functional theory within full potential method to investigate the influence of the phase transition on the electronic band structure, the angular momentum projected density of states, the electronic charge density distribution and the chemical bonding characters. In the recent years due to the improvement of the computational technologies, it has been proven that the first-principles calculation is one strong and useful tool to predict the crystal structure and its properties related to the electron configuration of a material before its synthesis [13–16].

2. Calculation methodology

It has been reported that during the synthesized of the polycrystalline $BaTeMo_2O_9$ a phase transition from β-$BaTeMo_2O_9$ to α-$BaTeMo_2O_9$ occurs at 570 °C [2]. The X-ray diffraction explore that, β-$BaTeMo_2O_9$ crystallized in monoclinic structure with space group $P2_1$, while α-$BaTeMo_2O_9$ crystallizes in orthorhombic $Pca2_1$ space group [2,17]. The crystal structure of β-$BaTeMo_2O_9$ and α-$BaTeMo_2O_9$ are shown in Fig. 1. More details about the crystals structures were presented in the captions of Fig. 1. The figure illustrated the MoO_6 and TeO_4 polyhedra of β-$BaTeMo_2O_9$ phase and the asymmetric unit with formula $BaTeMo_2O_9$, while for α-$BaTeMo_2O_9$ phase it shows the Mo_4O_{20} tetramer and the asymmetric unit with formula $Ba_2Te_2Mo_4O_{18}$. To investigate the electronic structure of

the two phases, the X-ray diffraction data obtained by Zhang et al. [2] were used as input data for comprehensive theoretical calculation. The experimental geometrical structure was optimized. The optimization were performed using the all-electron full potential linear augmented plane wave plus local orbitals ($FPLAPW + lo$) method as implemented in WIEN2k code [18] within generalized gradient approximation (PBE–GGA) [19]. The optimized geometrical structure exhibit good agreement with the experimental crystallographic data [2] as shown in Tables 1 and 2. The resulting relaxed geometry was used to calculated the electronic band structure, the angular momentum projected density of states, the electronic charge density distribution and the chemical bonding characters using PBE–GGA and the recently modified Becke–Johnson potential (mBJ) [20]. The modified Becke–Johnson potential allows the calculation with accuracy similar to the very expensive GW calculations [20]. It is a local approximation to an atomic "exact-exchange" potential and a screening term. Since the mBJ approach succeed by large amount in bringing the calculated energy gap closer to the experimental one therefore, we chose to present the results obtained by mBJ. The spherical harmonic expansion was used inside the non-overlapping spheres of muffin-tin radius (R_{MT}) and the plane wave basis set was chosen in the interstitial region (IR) of the unit cell. The R_{MT} for Ba, Mo, Te and O atoms were chosen in such a way that the spheres did not overlap, these values are 2.44 (2.47) a.u. for Ba $\beta(\alpha)$, 1.79 (1.83) a.u. for Te
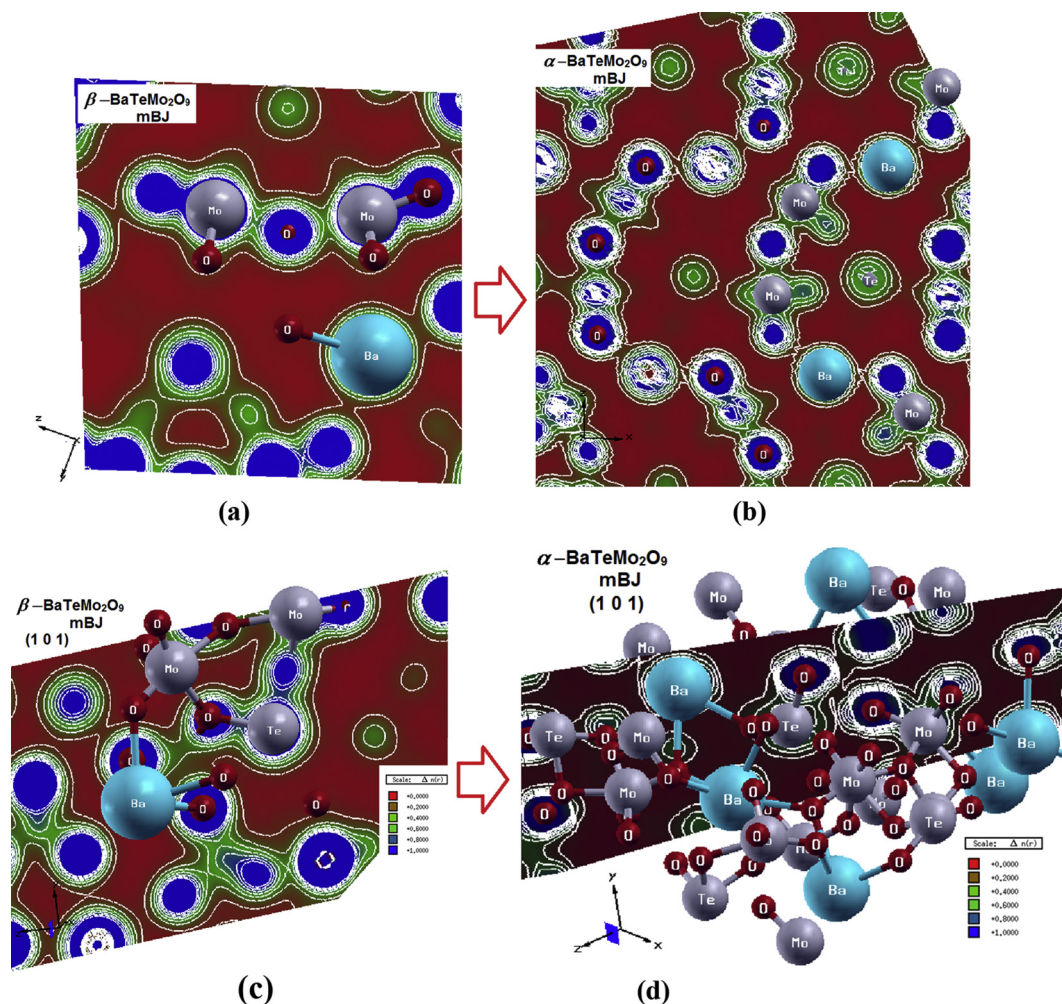

Fig. 4. Calculated electronic charge density distribution of β-$BaTeMo_2O_9$ and α-$BaTeMo_2O_9$ using mBJ; **(a)** crystallographic plan (1 0 0) for β-$BaTeMo_2O_9$; **(b)** crystallographic plan (1 0 0) for α-$BaTeMo_2O_9$; **(c)** crystallographic plan (1 0 1) for β-$BaTeMo_2O_9$; **(d)** crystallographic plan (1 0 1) for α-$BaTeMo_2O_9$.

β(α), 1.61 (1.62) for Mo β(α) and 1.46 for β(α) O. To achieve the total energy convergence, the basis functions in the *IR* were expanded up to $R_{MT} \times K_{max} = 7.0$ and inside the atomic spheres for the wave function. The maximum value of l was taken as $l_{max} = 10$, while the charge density is Fourier expanded up to $G_{max} = 12.0(a.u)^{-1}$. A self-consistency is obtained using 300 k points in the irreducible Brillouin zone (*IBZ*). The self-consistent calculations are converged since the total energy of the system is stable within 0.00001 *Ry*. The electronic band structures calculation are performed within 1500 k points in the *IBZ*.

3. Results and discussion

In order to explore and exploit the phase transition from β → α, the electronic band structure of the two phases were calculated and illustrated in Fig. 2(a,b). It has been found that both phases exhibit indirect band gap of about 2.93 eV (β) and 3.12 eV (α) in good agreement with the measured values 2.95 eV (β) and 3.12 eV (α) obtained from UV−Vis diffuse reflectance spectroscopy [2] (see Fig. 1S in the supplementary materials). Its clear that the *mBJ* approach succeed by large amount in bringing the calculated energy gap closer to the experimental one as we expected from this approach [21−23]. In both phases the conduction band minimum (CBM) is located at Γ point of the first *BZ* whereas the valence band maximum (VBM) of β-BaTeMo$_2$O$_9$ phase is situated in the mid way between Z and Γ, while it is located at Z point for α-BaTeMo$_2$O$_9$ phase. We set the zero-point of energy (Fermi level) at the valence band maximum. It is interesting to mention here that the phase transition from β → α turn the structure to be more complicated due to the appearance of Mo$_4$O$_{20}$ tetramer in α phase and the symmetric unit in α-phase became twice of that in β-phase as shown in Fig. 1. To carefully investigate the electronic structure and the role of the orbitals of each atom in both phases, the angular momentum projected density of states were investigated. Fig. 3(a) illustrated the total density of states of β-BaTeMo$_2$O$_9$ and α-BaTe-Mo$_2$O$_9$ phases which confirm the occurrence of the band gap enlargement. It has been noticed that the α-phase exhibits more pronounced structure in comparison to β-phase.

The angular momentum character of the various structures for the two phases can be obtained from calculating the angular momentum projected density of states (PDOS) as shown in Fig. 3(b–i). The structures confined between −10.0 and −9.0 eV are mainly belong to Ba-p, Ba-s states with small contribution of O-s/p states which show strong hybridization between Te-s and O-s/p states. The structure between −5.0 eV up to Fermi level (E$_F$) consist of Mo-d, Te-p/d and O-s/p states with insignificant contribution from Mo-s/p and Ba-s states, where Te-d state hybridized with O-s state while Ba-s state hybridized with Mo-s/p states. From the CBM and above there exists admixture of Mo-d, Ba-d, Te-s/p/d, O-s/p states with small contribution of Ba-s and Mo-s/p states. Due to shift the CBM towards higher energies during the phase transition from β → α, the whole structure of α-BaTeMo$_2$O$_9$ phase shifts towards higher energies by around 0.19 eV and the strong hybridization between Te-p and O-p states in β-phase become weaker in α-phase and the same for the hybridization between Te-d and O-s states. The strong hybridization may lead to form covalent bonding. Covalent bonding is more favorable for the transport of the carriers than ionic one [24].

The origin of chemical bonding can be elucidated from the angular momentum decomposition of the atoms projected electronic density of states. Integrating the latter from −6.0 eV up to E$_F$ we obtain the total number of electrons/eV (*e/eV*) for the orbitals in each atom of β-BaTeMo$_2$O$_9$ (α-BaTeMo$_2$O$_9$) phases, Mo-d state 2.0 *e/eV* (1.0 *e/eV*), O-p state 1.8 *e/eV* (2.9 *e/eV*), Te-p state 0.24 *e/eV* (0.25 *e/eV*), Mo-p state 0.07 *e/eV* (0.085 *e/eV*), Mo-s 0.03 *e/eV*

(0.035 *e/eV*), O-s state 0.02 *e/eV* (0.02 *e/eV*), Te-d state 0.015 *e/eV* (0.03 *e/eV*) and Ba-s state 0.01 *e/eV* (0.031 *e/eV*). The contributions of these orbitals to the valence bands exhibit that there are some electrons from Ba, Te, Mo and O atoms are transferred into valence bands and contribute in covalence interactions between the atoms. The covalent bond arises due to the degree of the hybridization and the electronegativity differences between the atoms. It is clear that there is an interaction of charges between the atoms due to the existence of the hybridization, showing that there is a strong/weak covalent bonding between these atoms. Thus the angular momentum decomposition of the atoms projected electronic density of states help us to analyze the nature of the bonds according to the classical chemical concept. This concept is very useful to classify compounds into different categories with respect to different

Table 3
The calculate bond lengths of α-BaTeMo$_2$O$_9$ and β-BaTeMo$_2$O$_9$ phases using mBJ in comparison with the experimental data [2].

Bond distances (Å)					
α-BaTeMo$_2$O$_9$			β-BaTeMo$_2$O$_9$		
	Exp.	This work		Exp.	This work
Ba1−O2	2.925681997	2.9255	Mo1−O1	2.225129892	2.2250
Ba1−O3	2.840259831	2.8422	Mo1−O3	2.214887592	2.2147
Ba1−O4	2.823452444	2.8243	Mo1−O4	1.816390444	1.8164
Ba1−O5	2.85532476	2.8556	Mo1−O5	1.734504233	1.7344
Ba1−O6	3.248935203	3.2488	Mo1−O6	1.739812255	1.7396
Ba1−O7	2.868854636	2.8689	Mo1−O7	2.053413137	2.0530
Ba1−O11	2.934993449	2.9350	Mo2−O1	2.13562646	2.1353
Ba1−O12	2.861002968	2.8611	Mo2−O2	2.152835459	2.1522
Ba1−O14	2.819479296	2.8192	Mo2−O3	2.199895839	2.1999
Ba1−O15	2.801490995	2.8021	Mo2−O7	1.826182531	1.8259
Ba2−O3	2.786285884	2.7860	Mo2−O8	1.720623555	1.7200
Ba2−O5	2.914002338	2.9151	Mo2−O9	1.741607882	1.7411
Ba2−O6	2.811971612	2.8120	Te1−O1	1.925602132	1.9255
Ba2−O7	2.97437665	2.9741	Te1−O2	1.865217501	1.8651
Ba2−O10	2.980174922	2.9811	Te1−O3	1.953020274	1.9531
Ba2−O11	2.899708292	2.8979	Te1−O4	2.347580339	2.3472
Ba2−O12	2.841345649	2.8420	Ba1−O2	2.739434972	2.7392
Ba2−O14	3.069378205	3.0693	Ba1−O4	3.078264767	3.0780
Ba2−O15	3.05152139	3.0514	Ba1−O4A	2.819174067	2.8190
Ba2−O16	2.774240224	2.7741	Ba1−O5	2.88593126	2.8860
Te1−O2	2.487646365	2.4874	Ba1−O5A	2.94351182	2.9431
Te1−O9	1.914757755	1.9146	Ba1−O6	3.221055998	3.2212
Te1−O10	1.911795147	1.9116	Ba1−O6A	3.192056172	3.1922
Te1−O11	1.920800578	1.9209	Ba1−O6B	2.805831505	2.8056
Te2−O2	1.920208559	1.9201	Ba1−O8	2.794255172	2.7944
Te2−O7	1.908995235	1.9088	Ba1−O9	2.736942151	2.7370
Te2−O18	1.910796233	1.9108	Ba1−O9A	3.001210142	3.0010
Mo1−O1	2.266280466	2.2665			
Mo1−O2	2.140925903	2.1407			
Mo1−O3	1.755002126	1.7551			
Mo1−O4	1.726743054	1.7265			
Mo1−O8	1.772189524	1.7725			
Mo1−O9	2.142715858	2.1429			
Mo2−O9	2.210507209	2.2100			
Mo2−O11	2.106590187	2.1069			
Mo2−O12	1.74462386	1.7449			
Mo2−O13	1.773708314	1.7731			
Mo2−O14	1.737578422	1.7372			
Mo2−O17	2.270906676	2.2711			
Mo3−O10	2.161429271	2.1610			
Mo3−O13	2.219661619	2.2192			
Mo3−O15	1.74487134	1.7444			
Mo3−O16	1.737120563	1.7373			
Mo3−O17	1.771040067	1.7711			
Mo3−O18	2.164155621	2.1643			
Mo4−O1	1.764790351	1.7641			
Mo4−O5	1.743439633	1.7432			
Mo4−O6	1.738550204	1.7391			
Mo4−O7	2.116563242	2.1160			
Mo4−O8	2.294844088	2.2946			
Mo4−O18	2.190510874	2.1901			

Table 4
The calculated bond angles of α-BaTeMo$_2$O$_9$ and β-BaTeMo$_2$O$_9$ phases using mBJ in comparison with the experimental data [2].

Bond angles (°)					
α-BaTeMo$_2$O$_9$			β-BaTeMo$_2$O$_9$		
Bond angles	Exp.	This work	Bond angles	Exp.	This work
O(8)–Mo(1)–O(2)	159.63(15)	159.59	O(4)–Mo(1)–O(7)#7	156.01(9)	156.02
O(3)–Mo(1)–O(9)	155.07(16)	155.00	O(5)–Mo(1)–O(3)#8	164.34(10)	164.30
O(4)–Mo(1)–O(1)	162.82(15)	162.77	O(6)–Mo(1)–O(1)	166.58(10)	166.60
O(13)–Mo(2)–O(11)	155.52(16)	155.53	O(9)–Mo(2)–O(1)#10	154.51(10)	154.48
O(12)–Mo(2)–O(9)	156.22(17)	156.25	O(7)–Mo(2)–O(2)#11	166.85(10)	166.80
O(14)–Mo(2)–O(17)#2	163.02(14)	163.03	O(8)–Mo(2)–O(3)#10	161.90(11)	161.91
O(17)–Mo(3)–O(10)#7	160.40(15)	160.35			
O(15)–Mo(3)–O(18)	157.17(17)	157.10			
O(16)–Mo(3)–O(13)	161.15(16)	161.11			
O(1)#8–Mo(4)–O(7)	155.12(16)	155.09			
O(5)–Mo(4)–O(18)	155.47(16)	155.41			
O(6)–Mo(4)–O(8)	162.27(15)	162.23			

chemical and physical properties.

With the aid of the calculated valence band's electronic charge density distribution, we obtained an image of the electron clouds that surround the molecules in the unit cell. We hope that this image will allow us to discuss the chemical bonding features. Therefore, we have taken a careful look at valence band's electronic charge density distribution to visualize the charge transfer and the chemical bonding characters of β-BaTeMo$_2$O$_9$ phase and the influence of the phase transition on the bonds characters of the resulting phase α-BaTeMo$_2$O$_9$. For this purpose the total valence charge density distribution in two crystallographic planes (1 0 0) and (1 0 1) were illustrated in Fig. 4(a–d). The crystallographic plane (1 0 0) of β-BaTeMo$_2$O$_9$ phase (Fig. 4a) show there exists a strong covalent bonding between Mo and O atoms due to small electronegativity differences between them. Also we can see the Ba atom forms mostly ionic and partially covalent bonding with O atom due to the large electronegativity difference. The phase transition from β → α cause to perturb the interaction between Mo and O atoms and between Ba and O atoms due to the different arrangement between the atoms, as it is clear from Fig. 4b. Deep insight into the electronic structure can be obtained from the crystallographic plane (1 0 1), β-phase exhibit a covalent bonding between Te and O atoms in addition to that between Mo and O atoms (Fig. 4c), the transition from β-to α-phase lead to weaken this interaction due to change the atoms arrangement (Fig. 4d). Due to the electronegativity difference between the atoms we can see a charge transfer towards O atoms as indicated by the blue color (in the web version) around O atoms (according to the thermoscale the blue color exhibit the maximum charge accumulation).

Since the unit cell of β-phase consists of two symmetry independent MoO$_6$ octahedra and one TeO$_4$ polyhedra and the asymmetric unit is BaTeMo$_2$O$_9$, while α-phase contains TeO$_3$, TeO$_4$ polyhedra and MoO$_6$ octahedra. It has been noticed that the MoO$_6$ octahedra combine with three unique MoO$_6$ nearest neighbors through the corners to form the tetramer Mo$_4$O$_{20}$ and the asymmetric unit is doubled in comparison to that of β-phase which make the structure complicated and influence the bond length, angles and characters in comparison to that of β-phase. Therefore, we have calculated the bond lengths and angles of the two phases as shown in Tables 3 and 4 and 5 in comparison with the measured one [2], good agreement was found.

4. Conclusions

A comprehensive ab-initio calculations were performed to investigate the electronic band structure, the angular momentum projected density of states, the electronic charge density distribution and the chemical bonding characters. We have used the reported experimental geometrical structure as input data for this calculation. The experimental geometrical structure was optimized by minimizing the forces acting on each atom. The optimization were performed using FPLAPW + lo method within PBE–GGA. The optimized geometrical structure show good agreement with the experimental crystallographic data. The resulting relaxed geometry was used to calculate the above mentioned properties using PBE–GGA and the recently modified Becke–Johnson potential (mBJ). Both phases exhibit an indirect band gap of about 2.93 eV (β) and 3.12 eV (α) in good agreement with the measured values 2.95 eV (β) and 3.12 eV (α). In both phases the O-p state form the VBM while Mo-d state exhibit the main contribution to the CBM.

It is interesting to mention here that the phase transition from β → α turn the structure to be more complicated due to the appearance of Mo$_4$O$_{20}$ tetramer in α phase and the symmetric unit in α-phase became twice of that in β-phase. The angular momentum projected density of states were calculated to investigated the role of the orbitals of each atom in both phases. The valence band's electronic charge density distribution reveals that the β-BaTeMo$_2$O$_9$ phase show there exists a strong covalent bonding between Mo and O atoms also between Te and O atoms, while Ba atom forms mostly ionic and partially covalent bonding with O atom. The phase transition from β → α cause to perturb the interaction between Mo and O atoms, Te and O atoms and between Ba and O atoms due to the different arrangement between the atoms. Due to the electro-negativity difference between the atoms we can see a charge transfer towards O atoms as indicated by the blue color around O atoms. The calculated bond lengths and angles show good agreement with the experimental values. The good agreement with experimental data in the matter of lattice parameters, energy gap values, the bond lengths and angles reveals the accuracy of the selected exchange correlation potentials used here.

Appendix A. Supplementary data

Supplementary data related to this article can be found at http://dx.doi.org/10.1016/j.jallcom.2015.08.142.

References

[1] (a) A. Authier, International Tables for Crystallography. Physical Properties of Crystals, Kluwer Academic Publishers, Dordrecht, The Netherlands, 2003 (Vol. D);
(b) J.F. Nye, Physical Properties of Crystals: Their Representation by Tensors and Matrices, Oxford University Press, New York, 1985;
(c) S.R. Marder, G.D. Stucky, J.E. Sohn, Materials for nonlinear optics: chemical perspectives, in: ACS Symposium Series, vol. 455, American Chemical Society, Washington, DC, 1991;
(d) R. Waser, U. Böttger, S. Tiedke, Polar Oxides: Properties, Characterization, and Imaging, Wiley-VCH Verlag GmbH & Co. KGaA, Weinheim, 2005.
[2] J. Zhang, Z. Zhang, W. Zhang, Q. Zheng, Y. Sun, C. Zhang, X. Tao, Chem. Mater 23 (2011) 3752–3837.
[3] A. Majchrowski, B. Sahraoui, A.O. Fedorchuk, L.R. Jaroszewicz, E. Michalski, A. Migalska-Zalas, I.V. Kityk, J. Mater. Sci. 48 (2013) 5938–5945.
[4] V. Kapustianyk, B. Turko, A. Kostruba, Z. Sofiani, B. Derkowska, S. Dabos-Seignon, B. Barwinski, Yu Eliyashevskyi, B. Sahraoui, Opt. Commun. 269 (2007) 346–350.
[5] S. Zongo, A.P. Kerasidou, B.T. Sone, A. Diallo, P. Mthunzi, K. Iliopoulos, M. Nkosi, M. Maaza, B. Sahraoui, Appl. Surf. Sci. 340 (2015) 72–77.
[6] A.H. Reshak, Xuean Chen, I.V. Kityk, S. Auluck, K. Iliopoulos, S. Couris, R. Khenata, Curr. Opin. Solid State Mater. Sci. 12 (2009) 26–31.
[7] Z.L. Gao, Q. Wu, X.T. Liu, Y.X. Sun, X.T. Tao, Opt. Express 23 (2015) 3851.
[8] (a) W. Zhang, X. Tao, C. Zhang, H. Zhang, M. Jiang, Cryst. Growth Des. 9 (2009) 2633–2636;
(b) W. Zhang, X. Tao, C. Zhang, Z.L. Gao, Y.Z. Zhang, W.T. Yu, X.F. Cheng, X.S. Liu, M.H. Jiang, Cryst. Growth Des. 8 (2008) 304–307.
[9] W. Zhang, F. Li, S.-H. Kim, P.S. Halasyamani, Cryst. Growth Des. 10 (2010) 4091–4095.
[10] J. Zhang, X. Tao, Y. Sun, Z. Zhang, C. Zhang, Z. Gao, H. Xia, S. Xia, Cryst. Growth Des. 11 (2011) 1863–1868.
[11] J. Zhang, Z. Zhang, Y. Sun, C. Zhang, X. Tao, CrystEngComm 13 (2011) 6985.
[12] Shan-De Liu, Ze-Liang Gao, Jun-Jie Zhang, Bai-Tao Zhang, Jing-Liang He, Xu-Tang Tao, IEEE Photonics Tech. Lett. 26 (2014) 15.
[13] A.H. Reshak, A. Majchrowski, M. Swirkowicz, A. Kłos, T. Łukasiewicz, I.V. Kityk, K. Iliopoulos, S. Couris, M.G. Brik, J. Alloys Compd. 481 (2009) 14–16.
[14] A.H. Reshak, S. Auluck, I.V. Kityk, J. Alloys Compd. 473 (2009) 20–24.
[15] K.J. Plucinski, I.V. Kityk, J. Kasperczyk, B. Sahraoui, Semicond. Sci. Technol. 16 (2001) 467–470.
[16] M. Malachowski, I.R. Kityk, B. Sahraoui, Phys. Lett. A 242 (1998) 337–342.
[17] W.G. Zhang, X.T. Tao, C.Q. Zhang, Z.L. Gao, Y.Z. Zhang, W.T. Yu, X.F. Cheng, X.S. Liu, M.H. Jiang, Cryst. Growth Des. 8 (2008) 304–307.
[18] P. Blaha, K. Schwarz, G.K.H. Madsen, D. Kvasnicka, J. Luitz, WIEN2k, an Augmented Plane Wave Plus Local Orbitals Program for Calculating Crystal Properties, Vienna University of Technology, Austria, 2001.
[19] J.P. Perdew, S. Burke, M. Ernzerhof, Phys. Rev. Lett. 77 (1996) 3865.
[20] F. Tran, P. Blaha, Phys. Rev. Lett. 102 (2009) 226401.
[21] A.H. Reshak, RSC Adv. 5 (2015) 22044.
[22] A.H. Reshak, Hongwei Huang, H. Kamarudin, S. Auluck, J. Appl. Phys. 117 (2015) 085703.
[23] A.H. Reshak, RSC Adv. 5 (2015) 33632.
[24] Fang Wu, Hong zhang Song, Jian feng Jia, Xing Hu, Prog. Nat. Sci. Mater. Int. 23 (4) (2013) 408–412.